Original Article

Comparison of knife-edge and multi-slit camera for proton beam range verification by Monte Carlo simulation

Jong Hoon Park [a], Sung Hun Kim [a], Youngmo Ku [a], Hyun Su Lee [a], Chan Hyeong Kim [a, *], Dong Ho Shin [b], Jong Hwi Jeong [c]

[a] Department of Nuclear Engineering, Hanyang University, Seoul, South Korea
[b] IT Convergence Technology Research Laboratory, Electronics and Telecommunications Research Institute, Daejeon, South Korea
[c] Proton Therapy Center, National Cancer Center, Goyang-si, Gyeonggi-do, South Korea

ABSTRACT

The mechanical-collimation imaging is the most mature technology in prompt gamma (PG) imaging which is considered the most promising technology for beam range verification in proton therapy. The purpose of the present study is to compare the performances of two mechanical-collimation PG cameras, knife-edge (KE) camera and multi-slit (MS) camera. For this, the PG cameras were modeled by Geant4 Monte Carlo code, and the performances of the cameras were compared for imaginary point and line sources and for proton beams incident on a cylindrical PMMA phantom. From the simulation results, the KE camera was found to show higher counting efficiency than the MS camera, being able to estimate the beam range even for 10^7 protons. Our results, however, confirmed that in order to estimate the beam range correctly, the KE camera should be aligned, at least approximately, to the location of the proton beam range. The MS camera was found to show lower efficiency, being able to estimate the beam range correctly only when the number of the protons is at least 10^8. For enough number of protons, however, the MS camera estimated the beam range correctly, errors being less than 1.2 mm, regardless of the location of the camera.

© 2018 Korean Nuclear Society, Published by Elsevier Korea LLC. This is an open access article under the CC BY-NC-ND license (http://creativecommons.org/licenses/by-nc-nd/4.0/).

1. Introduction

The main advantage of proton therapy over conventional X-ray and electron beam therapy is the high-gradient dose distribution at the end of the proton beam range, which provides highly conformal radiation dose to the tumor volume, sparing surrounding normal tissue and critical structures. Because of the advantage, the numbers of proton therapy centers and the patients treated with proton therapy are rapidly increasing. Despite the advantage and the increasing interest in proton therapy, however, there is still a critical issue that has to be addressed to maximize the efficiency of therapy and the safety of the patient. That is, we should be able to measure the proton beam range in the patient, preferentially in real time [1].

Because the proton beam completely stops in the patient, the secondary radiations generated from the proton beam passage in the patient are utilized to locate the proton beam range. Note that

the range is defined as the depth or the location of distal 90% dose in a depth-dose curve. There have been several studies on prompt-gamma (PG) measurement for real-time measurement of the proton beam range in the patient [2]. The first feasibility study was done by Min et al. [3], who used a single slit collimator and a single detector. Currently, many research groups are developing PG measurement systems for beam range verification or measurement based on different technologies, such as mechanical collimation imaging [4–6], Compton imaging [7–9], prompt gamma timing (PGT) [10], prompt gamma peak integration (PGPI) [11], and prompt gamma spectroscopy (PGS) [12]. The Compton imaging, PGT, PGPI, and PGS have their own advantages but have not yet matured to be applied to patient treatment. The conventional mechanical-collimation imaging provides only one-dimensional dose information, but we still believe it is the most mature and promising technology at present due to the high counting efficiency and the high accuracy of the determined proton beam range.

In the present study, we compared two mechanical-collimation cameras, knife-edge (KE) and multi-slit (MS) camera, which have been proposed by researchers [4,6,13,14]. Even though the KE and

MS camera have been compared by some research groups in the past [15,16], the comparisons are not considered fair in that the MS camera in comparison was not an optimized system while the KE camera was a fully optimized system. In the present study, we compared the performances of the KE camera optimized by Perali et al. [4] and the MS camera optimized by Park et al. [17]. For this, these cameras were modeled by Geant4 Monte Carlo code [18], and the performances of the cameras were simulated and compared for imaginary point and line sources and for proton beams incident on a cylindrical PMMA phantom.

2. Material and methods

2.1. Monte Carlo simulation

The Geant4 (version 10.03.p01) Monte Carlo simulation toolkit was used to simulate the KE and MS camera for measuring PGs. For hadron physics, the QGSP_BERT_HP physics list was chosen, which shows a good agreement with the measurement of prompt gammas. The simulations also used the physics models of G4EmStandardPhysics_option4, G4HadronElasticPhysics, G4IonElasticPhysics, and G4IonPhysics, G4DecayPhysics, and G4StoppingPhysics. The range cut-off for proton, electron, positron, and photon was set to be 0.1 mm. Variance reduction technics (VRTs) were not used. The computer used for the simulations had a CPU with an Intel® Xeon® Processor E5-2697 v2 with 256 GB of memory and operated on the CentOS7 operating system.

2.2. Knife-edge (KE) and multi-slit (MS) camera

Fig. 1 shows the knife-edge (KE) camera, which consists of a KE collimator and two rows of 20 LYSO scintillations, as described in Perali et al. [4]. The KE collimator is made of tungsten (16.96 g/cm^3) with 40 mm thickness, 63° slit angle, 6 mm slit width, and 120 mm height. Each of the 40 LYSO scintillators (Lu$_{1.8}$Y$_{0.2}$SiO$_5$:Ce, 7.1 g/cm^3) has a size of 4 mm (thickness) × 30 mm (width) × 100 mm (height). The 40 LYSO scintillators are located at a distance of 200 mm from the center of the collimator (see Fig. 1). The camera register a count if a gamma ray deposits 3—6 MeV to one of the detectors.

Fig. 2 shows the multi-slit (MS) camera, which consists of an MS collimator and two rows of 36 CsI(Tl) scintillators. The MS collimator is made of tungsten, and both the slit width and septal thickness are 2 mm. The height of the slits is 100 mm to match the height of the CsI(Tl) scintillators. The length of the slit is 100 mm. To overcome the physical limitations of the 4 mm slit pitch, the multi-slit collimator is placed in a staggered arrangement (see Fig. 2, side view), which provides 2 mm measurement pitch. The 72 CsI(Tl) scintillators (4.51 g/cm^3) of 3 mm (thickness) × 30 mm (width) × 100 mm (height) are located right behind the slits of the collimator. The energy window of the MS camera was set to that of the KE camera; that is, the MS camera is set to register a count if a gamma ray deposits 3—6 MeV to one of the detectors.

2.3. Curve fitting methods

Fig. 3 shows the curve fitting methods used with the KE and MS camera to determine the range (i.e., absolute range) of the proton beam. The 3-line-segment fitting is used for the KE camera to determine the range of the proton beam, as described in Smeet et al. [19]. The 3-line-segment curve is defined by four points, and the first and fourth point are set to the first and last positions of the PG distribution, respectively. The second point and the third point are selected to best fit the measured distribution of prompt gammas. From these characteristic points, the location of the absolute range is determined as the middle of the second and the third points.

The sigmoidal curve fitting is used for the MS camera to determine the range of the proton beam. For this, the fitting window, to apply the sigmoidal curve fitting, is determined as follows. The start point of the fitting window is determined as 10 mm in front of the maximum peak of the distribution which was produced by applying the 8-point moving average filter on the PG distribution. The endpoint of the fitting window is determined as 40 mm behind the falloff point determined by the method of Sobel edge detection. After the determination of the fitting window, the sigmoidal curve fitting is applied to the fitting window in the PG distribution, after applying the median filter to the original PG distribution to remove the statistic noise. The inflection point of the sigmoidal curve is then taken as the location of the proton beam range.

3. Results and discussion

In the present study, the performances of the KE and MS cameras were compared by simulating therapeutic proton beams incident on a cylindrical PMMA phantom. Before these simulation with therapeutic proton beams, however, we first compared the performances of the KE and MS camera for simple imaginary point and line sources for more intuitive comparison. Fig. 4 shows the simulation geometry for the point source. The point source is assumed to emit prompt gammas with the same energies and emission yields of the PGs, for the energies greater than 3 MeV, which are generated when a 150 MeV proton beam is irradiated to a PMMA phantom. The point source was assumed to be positioned at different locations, with the separation distance of the source (from
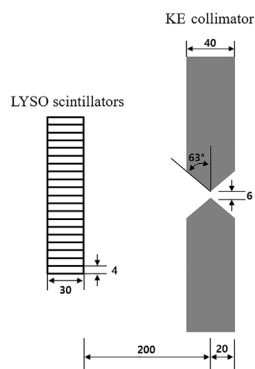

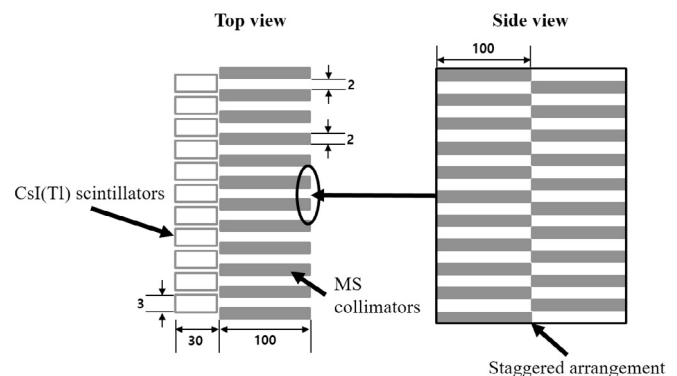**Fig. 1.** The knife-edge (KE) camera. The dimensions are in millimeters.

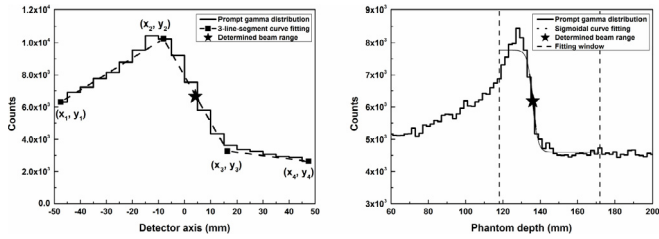**Fig. 2.** The multi-slit (MS) camera. The dimensions are in millimeters.

Fig. 3. Curve fitting methods: 3-line-segment fitting (left) and sigmoidal curve fitting (right).

the collimator surface) changing from 130, 180, 230, 280, to 330 mm and the displacement distance changing from 0, 10, 20, 30, 40, 50, to 60 mm. Note that the displacement distance is the distance from the reference point which is the center of the collimator and the center of the 6th collimator slit for the KE and MS camera, respectively. The simulation was performed for each of the source positions. For each simulation, enough number of source particles ($= 10^9$ prompt gammas) were simulated to eliminate the effect of statistics. Note that a complete stopping of a 150 MeV proton in a PMMA produces, on the average, 6.6×10^{-2} prompt gammas whose energies are higher than 3 MeV.

Fig. 5 shows the simulated PG images for the KE and MS camera for the source positions at the separation distance of 230 mm. For the KE camera, the center of the peaks, obtained from Gaussian fitting to the images, was found at 0.0, 10.7, 21.2, 31.9, and 42.3 mm, for the displacement distances of 0, 10, 20, 30, and 40 mm, respectively. The results show that, except for the point source located at the center of the KE collimator (i.e., displacement distance = 0.0 mm), the peaks are found at different locations, by up to 2.3 mm, when compared to the positions of the point source. The image was not obtained for the point source at 50 and 60 mm of displacement distance due to the limited FOV of the KE camera. The resolutions, in full width at half maximum (FWHM), of the images were within the range of 21.1–23.2 mm considering all source locations. The counting efficiencies were within the range of $4.1 \times 10^{-4} - 5.3 \times 10^{-4}$. For the MS camera, the center of the peaks was always observed at the source locations, within 0.1 mm of error, considering all source locations. The image

resolutions and counting efficiencies were 7.4 mm (FWHM) and $1.5 \times 10^{-4} - 2.6 \times 10^{-4}$, respectively, considering all source locations.

Table 1 summarizes the results of peak positions and image resolutions for the entire source locations considered in the present study. The hyphens ('-') in the table means that a valid image is not obtained for the given condition (i.e., separation and displacement distances). The table shows that FOV decreases with the decrease of separation distance for the KE camera while FOV does not change for the MS camera.

For the KE camera, except for the point source located at the center of the collimator (i.e., displacement distance = 0 mm), the peaks are found at different locations, by up to 3.2 mm, when compared to the positions of the point source. For the MS camera, the peaks were observed at the source locations, within 0.1 mm of error, considering all source locations.

The FHWM values are within the range of 17.9–28.2 mm and 4.7–8.9 mm for the KE and MS cameras, respectively. For both cameras, the FWHM value does not significantly change with the displacement distance, but significantly changes with the separation distance. For example, the FWHM value increases by 1.6 and 2.1 times when the separation distance changes from 130 to 330 mm for the KE and MS camera, respectively, for the displacement distance of 0 mm.

The counting efficiency is within the range of $0.2 \times 10^{-3} - 1.1 \times 10^{-3}$ and $1.8 \times 10^{-4} - 4.0 \times 10^{-4}$ for the KE and MS camera, respectively. The counting efficiencies also significantly change with the separation distance, but hardly change with the displacement distance for both cameras. The counting efficiency decreases by 3.4 and 2.0 times when the separation distance changes from 130 to 330 mm for the displacement distance of 0 mm. In general, the counting efficiency of the MS camera is lower by 1.2–3.1 times when compared to the KE camera considering all source locations.

The performances of the cameras were also compared for an imaginary line source emitting prompt gammas. For this, a 50 mm-long line source located at 230 mm away from the surface of the collimator (i.e., separation distance = 230 mm) was assumed to be imaged with the KE and MS camera (see Fig. 4). For each simulation, again enough number of source particles (i.e., 10^9 prompt gammas) were simulated to eliminate the effect of statistics. Fig. 6 shows the simulated PG images for the KE and MS camera for the line source. The image of the MS camera was found to show a higher gradient at the end of the line source, as expected from the point source results, better representing the shape of the line source. For distance (d) > 20 mm, on the other hand, the MS camera shows quite a high level of counts (~20% of the maximum counts), which indicates that the MS camera will suffer from high level of background counts when the MS camera is used for therapeutic proton beams. Note that in real proton therapy, the patient and the treatment room will be inundated by the capture gammas produced from neutron captures.
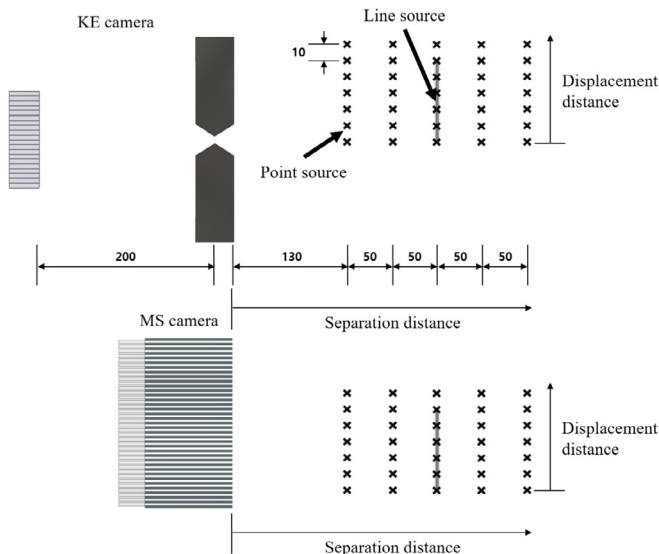

Fig. 4. Simulation geometry for point and line source. The dimensions are in millimeters.
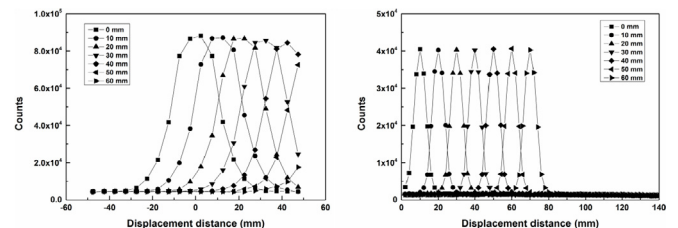

Fig. 5. The simulated PG images for the KE (left) and MS camera (right) for the point source at different displacement distance (0, 10, 20, 30, 40, 50, and 60 mm). The separation distance is 230 mm.

Table 1
Estimated peak positions, image resolutions (in FWHM), and efficiencies for the imaginary point source at different locations.

Camera	Separation distance	Estimation parameters	Displacement distance						
			0 mm	10 mm	20 mm	30 mm	40 mm	50 mm	60 mm
KE	130 mm	Peak pos. (mm)	0.0	10.6	21.2	–	–	–	–
		Image resol. (mm)	18.0	17.9	18.0				
		Efficiency	1.1×10^{-3}	1.0×10^{-3}	9.2×10^{-4}				
	180 mm	Peak pos. (mm)	0.0	10.6	21.2	31.9			
		Image resol. (mm)	20.6	20.5	20.2	20.3	–	–	–
		Efficiency	7.2×10^{-4}	7.2×10^{-4}	7.0×10^{-4}	5.9×10^{-4}			
	230 mm	Peak pos. (mm)	0.0	10.7	21.2	31.9	42.3		
		Image resol. (mm)	23.2	23.2	22.9	22.6	21.1	–	–
		Efficiency	5.3×10^{-4}	5.3×10^{-4}	5.2×10^{-4}	5.0×10^{-4}	4.1×10^{-4}		
	280 mm	Peak pos. (mm)	0.0	10.6	21.3	31.9	42.5	52.3	
		Image resol. (mm)	25.9	25.6	25.5	25.2	25.0	23.5	–
		Efficiency	4.1×10^{-4}	4.0×10^{-4}	4.0×10^{-4}	3.9×10^{-4}	3.7×10^{-4}	3.0×10^{-4}	
	330 mm	Peak pos. (mm)	0.0	10.6	21.2	31.9	42.7	53.2	62.3
		Image resol. (mm)	28.5	28.1	28.2	27.8	27.7	27.7	24.5
		Efficiency	3.2×10^{-4}	3.2×10^{-4}	3.2×10^{-4}	3.1×10^{-4}	3.1×10^{-4}	2.9×10^{-4}	2.2×10^{-4}
MS	130 mm	Peak pos. (mm)	0.0	10.0	20.0	30.0	40.0	50.0	60.0
		Image resol. (mm)	4.8	5.2	4.7	5.2	4.8	5.2	4.7
		Efficiency	3.6×10^{-4}	3.8×10^{-4}	3.8×10^{-4}	3.9×10^{-4}	3.9×10^{-4}	4.0×10^{-4}	4.0×10^{-4}
	180 mm	Peak pos. (mm)	0.0	10.0	20.0	30.0	40.0	50.0	60.0
		Image resol. (mm)	6.3	6.3	6.3	6.3	6.3	6.3	6.3
		Efficiency	3.0×10^{-4}	3.1×10^{-4}	3.1×10^{-4}	3.1×10^{-4}	3.2×10^{-4}	3.2×10^{-4}	3.2×10^{-4}
	230 mm	Peak pos. (mm)	0.0	10.0	20.0	30.0	40.0	50.0	60.0
		Image resol. (mm)	7.4	7.4	7.4	7.4	7.4	7.4	7.4
		Efficiency	2.5×10^{-4}	2.5×10^{-4}	2.6×10^{-4}	2.6×10^{-4}	2.6×10^{-4}	2.6×10^{-4}	2.6×10^{-4}
	280 mm	Peak pos. (mm)	0.0	10.0	20.0	30.0	40.0	50.0	60.0
		Image resol. (mm)	8.6	8.6	8.6	8.6	8.6	8.6	8.6
		Efficiency	2.1×10^{-4}	2.1×10^{-4}	2.2×10^{-4}	2.2×10^{-4}	2.2×10^{-4}	2.2×10^{-4}	2.2×10^{-4}
	330 mm	Peak pos. (mm)	0.0	10.0	20.0	30.0	40.0	50.0	60.0
		Image resol. (mm)	9.9	9.8	9.8	9.8	9.8	9.8	9.8
		Efficiency	1.8×10^{-4}	1.8×10^{-4}	1.8×10^{-4}	1.8×10^{-4}	1.9×10^{-4}	1.9×10^{-4}	1.9×10^{-4}

3.1. Therapeutic proton beam incident on a PMMA phantom

To compare the performances of the KE and MS camera for therapeutic proton beams, simulations were performed for a therapeutic proton beam incident on a cylindrical phantom which is made of PMMA (density = 1.19 g/cm^3) and has the dimensions of 300 mm (diameter) and 400 mm (length). Fig. 7 shows the geometry of PG imaging for therapeutic proton beam (pencil beam) incident on the center of the cylindrical phantom for the KE camera MS camera. For the KE camera, the distance between the beam and the surfa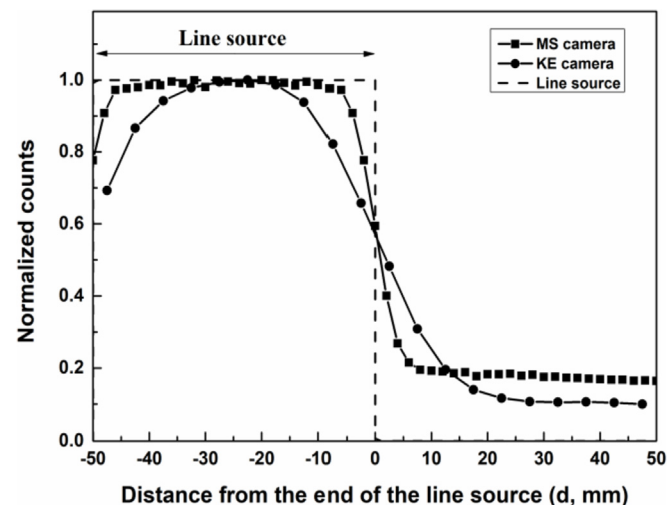ce of the collimator was set to 230 mm in order to keep a 5:4 magnification ratio corresponding to a field of view (FOV) of 100 mm along the beam axis [4]. For the MS camera, the distance between the beam and the surface of the collimator was also set to 230 mm to have the same measurement condition with the KE camera. For the KE camera, the center of the camera was aligned with the expected location of the beam range. For the MS, the position of the camera is not important, but also aligned with the location of the beam range to keep the same measurement condition.

Fig. 8 shows the simulated PG images for the KE and MS camera for 150 MeV proton beam incident on the cylindrical phantom. The simulations were done for different numbers of protons (10^9, 10^8, and 10^7) delivered to the phantom. Each simulation was repeated 10 times to get the mean and standard deviation of counts at each point, which is plotted in the figure. Note that the real range, which is defined as the depth or location of distal 90% dose in a depth-dose curve, is 133.9 mm for the 150 MeV proton beam. The KE camera estimated the range as 134.4 ± 0.2, 132.1 ± 0.7, and 130.9 ± 1.9 mm for 10^9, 10^8, and 10^7 protons. The MS camera estimated the range as 134.2 ± 0.4 and 135.5 ± 1.5 mm for 10^9 and 10^8 protons, and the MS camera could not estimate range for 10^7 protons due to low statistics. The result shows that for the number of protons equal to or greater than 10^8, both the cameras estimate the beam range within 2 mm of error. The KE camera is better from a statistical point of view even though for this result, the location of the KE camera should be adjusted so that the center of the camera is aligned, at least approximately, to the expected location of the range.

Fig. 9 shows the simulated PG images for the KE (left) and MS (right) camera which were obtained changing the energy of the proton beam. The energies simulated in the present study were 122.7, 136.8, 150.0, 162.4, and 174.2 MeV, which correspond to the beam ranges of 93.9, 113.9, 133.9, 153.9, and 173.9 mm, respectively.
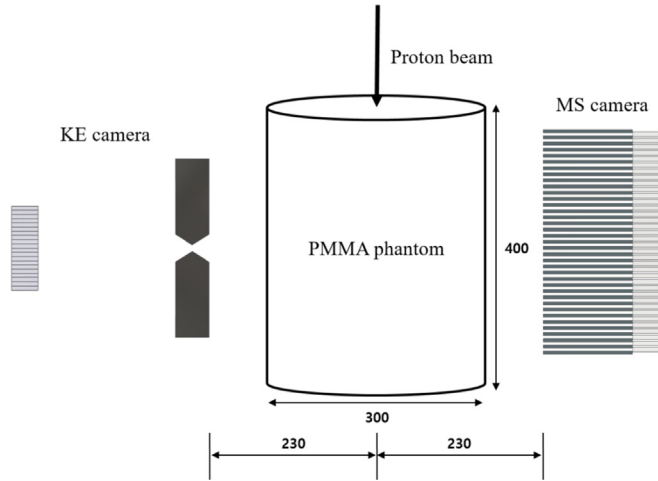

Fig. 6. The simulated PG images for the KE and MS camera for an imaginary line source with 50-mm long. The dash line shows the source distribution of the line source.

Fig. 7. Simulation geometry of PG imaging for therapeutic proton beam incident on cylindrical PMMA phantom for KE camera (left) and MS camera (right).
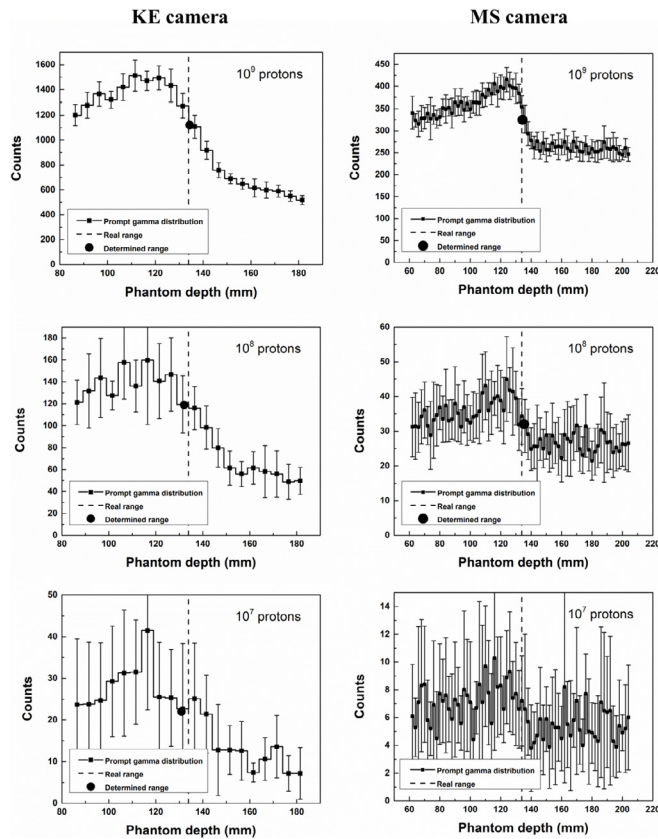

Fig. 8. The simulated PG images for the KE (left) and MS (right) camera for 150 MeV proton beam incident on a cylindrical PMMA phantom.

Again, each simulation was repeated 10 times to get the mean and standard deviation of counts at each point, which is plotted in the figure. Note that the cameras are now aligned with the beam range location of the 150 MeV beam. 10^9 protons were simulated for each case.

The KE camera estimated the beam range as 100.8 ± 0.3, 116.5 ± 0.2, 134.4 ± 0.2, 159.6 ± 0.4 mm for 122.7, 136.8, 150.0, and 162.4 MeV proton beams or for the real ranges of 93.9, 113.9, 133.9, 153.9, and 173.9 mm, respectively. This result shows that the KE
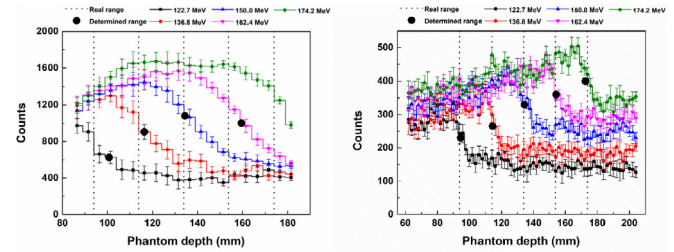

Fig. 9. The simulated PG images for the KE (left) and MS (right) camera for different proton energies. The figure shows the range (black filled square) determined by the 3-line-segment and sigmoidal curve fitting (right). The dotted vertical lines show the locations of the real range for comparison.

camera estimates the beam range correctly only when the KE camera is aligned with the location of the beam range. In the present study, the KE camera correctly estimated the beam range only for the 150 MeV proton beam for which the camera is aligned.

On the other hand, the MS camera estimates the beam range correctly for all proton beam energies considered in the present study. The MS camera estimated the beam range as 94.7 ± 0.4, 114.4 ± 0.4, 134.4 ± 0.4, 154.3 ± 0.4, and 172.7 ± 0.4 mm for the real ranges of 93.9, 113.9, 133.9, 153.9, and 173.9 mm, respectively, errors being less than 1.2 mm considering all proton beam energies. This result confirms that we do not need to align the MS camera to the location of the beam range, which is a significant advantage of the MS camera over the KE camera, especially in pencil beam scanning (PBS) proton therapy in which the energy of the proton beam changes continuously and rapidly during the treatment. Note that at present the PBS proton therapy is considered the most promising technology in proton therapy [20].

4. Conclusions

In the present study, the performances of the KE and MS camera were compared by Geant4 Monte Carlo simulations for proton beam range measurement in proton therapy. Our simulation results generally show that the KE camera shows higher counting efficiency, being able to estimate the beam range even for 10^7 protons for a spot. The results, however, also confirms that in order to estimate the beam range correctly, the KE camera should be aligned, at least approximately, to the location of the proton beam range, which is the main drawback of the camera, especially when we consider that the energy of the proton beam changes continuously and rapidly during pencil beam scanning (PBS) proton therapy which is at present considered the most promising technology in proton therapy. On the other hand, the MS camera shows lower efficiency when compared to the KE camera and the MS camera can estimate the beam range correctly only when the number of the protons is at least 10^8, which is a main drawback of the MS camera. For enough number of protons, the MS camera was found to estimate the beam range correctly, errors being less than 1.2 mm, for all the source locations considered in the present study. Note that the FOV of the MS camera can be expanded simply by using more detectors. The issue of low statistics for the MS camera could be addressed by using more protons for each spot (i.e., hypo-fractionation or using larger spots with more protons) or by merging the images of neighboring spots.

References

[1] A.C. Knopf, A. Lomax, In vivo proton range verification: a review, Phys. Med. Biol. 58 (2013).

[2] J. Krimmer, D. Dauvergne, J.M. Létang, É. Testa, Prompt-gamma monitoring in hadrontherapy: a review, Nucl. Instrum. Meth. Phys. Res. Sect. A Accel. Spectrom. Detect. Assoc. Equip. 878 (2018) 58—73.

[3] C.H. Min, C.H. Kim, M.Y. Youn, J.W. Kim, Prompt gamma measurements for locating the dose falloff region in the proton therapy, Appl. Phys. Lett. 89 (2006).

[4] I. Perali, A. Celani, L. Bombelli, C. Fiorini, F. Camera, E. Clementel, S. Henrotin, G. Janssens, D. Prieels, F. Roellinghoff, J. Smeets, F. Stichelbaut, F.V. Stappen, Prompt gamma imaging of proton pencil beams at clinical dose rate, Phys. Med. Biol. 59 (2014) 5849—5871.

[5] F. Roellinghoff, A. Benilov, D. Dauvergne, G. Dedes, N. Freud, G. Janssens, J. Krimmer, J.M. Letang, M. Pinto, D. Prieels, C. Ray, J. Smeets, F. Stichelbaut, E. Testa, Real-time proton beam range monitoring by means of prompt-gamma detection with a collimated camera, Phys. Med. Biol. 59 (2014).

[6] C.H. Min, H.R. Lee, C.H. Kim, S.B. Lee, Development of array-type prompt gamma measurement system for in vivo range verification in proton therapy, Med. Phys. 39 (2012) 2100—2107.

[7] T. Kormoll, F. Fiedler, C. Golnik, K. Heidel, M. Kempe, S. Schoene, M. Sobiella, K. Zuber, W. Enghardt, A prototype compton camera for in-vivo dosimetry of ion beam cancer irradiation, in: IEEE Nuclear Science Symposium Conference Record, 2012, pp. 3484—3487.

[8] J.C. Polf, S. Avery, D.S. Mackin, S. Beddar, Imaging of prompt gamma rays emitted during delivery of clinical proton beams with a Compton camera: feasibility studies for range verification, Phys. Med. Biol. 60 (2015) 7085—7099.

[9] J. Krimmer, J.L. Ley, C. Abellan, J.P. Cachemiche, L. Caponetto, X. Chen, M. Dahoumane, D. Dauvergne, N. Freud, B. Joly, D. Lambert, L. Lestand, J.M. Letang, M. Magne, H. Mathez, V. Maxim, G. Montarou, C. Morel, M. Pinto, C. Ray, V. Reithinger, E. Testa, Y. Zoccarato, Development of a Compton camera for medical applications based on silicon strip and scintillation detectors, Nucl. Instrum. Methods Phys. Res. Sect. A Accel. Spectrom. Detect. Assoc. Equip. 787 (2015) 98—101.

[10] C. Golnik, F. Hueso-Gonzalez, A. Muller, P. Dendooven, W. Enghardt, F. Fiedler, T. Kormoll, K. Roemer, J. Petzoldt, A. Wagner, G. Pausch, Range assessment in particle therapy based on prompt gamma-ray timing measurements, Phys. Med. Biol. 59 (2014) 5399—5422.

[11] J. Krimmer, G. Angellier, L. Balleyguier, D. Dauvergne, N. Freud, J. Hérault, J.M. Létang, H. Mathez, M. Pinto, E. Testa, Y. Zoccarato, A cost-effective monitoring technique in particle therapy via uncollimated prompt gamma peak integration, Appl. Phys. Lett. 110 (2017).

[12] J.M. Verburg, H.A. Shih, J. Seco, Simulation of prompt gamma-ray emission during proton radiotherapy, Phys. Med. Biol. 57 (2012) 5459—5472.

[13] V. Bom, L. Joulaeizadeh, F. Beekman, Real-time prompt gamma monitoring in spot-scanning proton therapy using imaging through a knife-edge-shaped slit, Phys. Med. Biol. 57 (2012) 297—308.

[14] J. Krimmer, M. Chevallier, J. Constanzo, D. Dauvergne, M. De Rydt, G. Dedes, N. Freud, P. Henriquet, C. La Tessa, J.M. Létang, R. Pleskac, M. Pinto, C. Ray, V. Reithinger, M.H. Richard, I. Rinaldi, F. Roellinghoff, C. Schuy, E. Testa, M. Testa, Collimated prompt gamma TOF measurements with multi-slit multi-detector configurations, J. Instrum. 10 (2015).

[15] J. Smeets, F. Roellinghoff, G. Janssens, I. Perali, A. Celani, C. Fiorini, N. Freud, E. Testa, D. Prieels, Experimental comparison of knife-edge and multi-parallel slit collimators for prompt gamma imaging of proton pencil beams, Front. Oncol. 6 (2016).

[16] H.H. Lin, H.T. Chang, T.C. Chao, K.S. Chuang, A comparison of two prompt gamma imaging techniques with collimator-based cameras for range verification in proton therapy, Radiat. Phys. Chem. 137 (2017) 144—150.

[17] J.H. Park, H.R. Lee, S.H. Kim, C.H. Kim, Y. Ku, D.H. Shin, J.H. Jeong, S.B. Lee, Construction and Test of Proof-of-principle Multi-slit Camera for Proton Beam Range Verification, PTCOG55, 2016, p. 312.

[18] S. Agostinelli, J. Allison, K. Amako, J. Apostolakis, H. Araujo, P. Arce, M. Asai, D. Axen, S. Banerjee, G. Barrand, F. Behner, L. Bellagamba, J. Boudreau, L. Broglia, A. Brunengo, H. Burkhardt, S. Chauvie, J. Chuma, R. Chytracek, G. Cooperman, G. Cosmo, P. Degtyarenko, A. Dell'Acqua, G. Depaola, D. Dietrich, R. Enami, A. Feliciello, C. Ferguson, H. Fesefeldt, G. Folger, F. Foppiano, A. Forti, S. Garelli, S. Giani, R. Giannitrapani, D. Gibin, J.J. Gomez Cadenas, I. Gonzalez, G. Gracia Abril, G. Greeniaus, W. Greiner, V. Grichine, A. Grossheim, S. Guatelli, P. Gumplinger, R. Hamatsu, K. Hashimoto, H. Hasui, A. Heikkinen, A. Howard, V. Ivanchenko, A. Johnson, F.W. Jones, J. Kallenbach, N. Kanaya, M. Kawabata, Y. Kawabata, M. Kawaguti, S. Kelner, P. Kent, A. Kimura, T. Kodama, R. Kokoulin, M. Kossov, H. Kurashige, E. Lamanna, T. Lampen, V. Lara, V. Lefebure, F. Lei, M. Liendl, W. Lockman, F. Longo, S. Magni, M. Maire, E. Medernach, K. Minamimoto, P. Mora de Freitas, Y. Morita, K. Murakami, M. Nagamatu, R. Nartallo, P. Nieminen, T. Nishimura, K. Ohtsubo, M. Okamura, S. O'Neale, Y. Oohata, K. Paech, J. Perl, A. Pfeiffer, M.G. Pia, F. Ranjard, A. Rybin, S. Sadilov, E. di Salvo, G. Santin, T. Sasaki, N. Savvas, Y. Sawada, S. Scherer, S. Sei, V. Sirotenko, D. Smith, N. Starkov, H. Stoecker, J. Sulkimo, M. Takahata, S. Tanaka, E. Tcherniaev, E. Safai Tehrani, M. Tropeano, P. Truscott, H. Uno, L. Urban, P. Urban, M. Verderi, A. Walkden, W. Wander, H. Weber, J.P. Wellisch, T. Wenaus, D.C. Williams, D. Wright, T. Yamada, H. Yoshida, D. Zschiesche, GEANT4 - a simulation toolkit, Nucl. Instrum. Methods Phys. Res. Sect. A Accel. Spectrom. Detect. Assoc. Equip. 506 (2003) 250—303.

[19] J. Smeets, F. Roellinghoff, D. Prieels, F. Stichelbaut, A. Benilov, P. Busca, C. Fiorini, R. Peloso, M. Basilavecchia, T. Frizzi, J.C. Dehaes, A. Dubus, Prompt gamma imaging with a slit camera for real-time range control in proton therapy, Phys. Med. Biol. 57 (2012) 3371—3405.

[20] L. Grevillot, D. Bertrand, F. Dessy, N. Freud, D. Sarrut, A Monte Carlo pencil beam scanning model for proton treatment plan simulation using GATE/GEANT4, Phys. Med. Biol. 56 (2011) 5203—5219.